

Dual-Regulation Strategy to Improve Anchoring and Conversion of Polysulfides in Lithium–Sulfur Batteries

Suya Zhou,[#] Shuo Yang,[#] Xinwei Ding, Yuchong Lai, Huagui Nie, Yonggui Zhang, Dan Chan, Huan Duan, Shaoming Huang, and Zhi Yang*



Cite This: *ACS Nano* 2020, 14, 7538–7551



Read Online

ACCESS |



Metrics & More



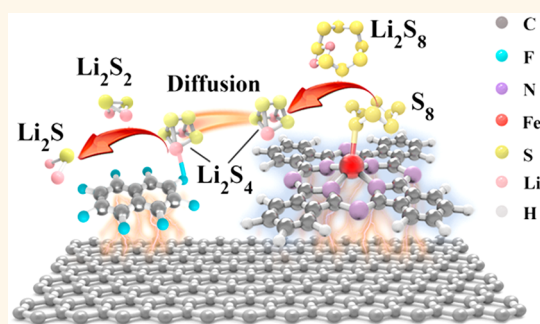
Article Recommendations



Supporting Information

ABSTRACT: The sluggish reaction kinetics at the cathode/electrolyte interface of lithium–sulfur (Li–S) batteries limits their commercialization. Herein, we show that a dual-regulation system of iron phthalocyanine (FePc) and octafluoronaphthalene (OFN) decorated on graphene (Gh), denoted as Gh/FePc+OFN, accelerates the interfacial reaction kinetics of lithium polysulfides (LiPSs). Multiple *in situ* spectroscopy techniques and *ex situ* X-ray photoelectron spectroscopy combined with density functional theory calculations demonstrate that FePc acts as an efficient anchor and scissor for the LiPSs through Fe⋯S coordination, mainly facilitating their liquid–liquid transformation, whereas OFN enables Li-bond interaction with the LiPSs, accelerating the kinetics of the liquid–solid nucleation and growth of Li₂S. This dual-regulation system promotes the smooth conversion reaction of sulfur, thereby improving the battery performance. A Gh/FePc+OFN-based Li–S cathode delivered an ultrahigh initial capacity of 1604 mAh g⁻¹ at 0.2 C, with an ultralow capacity decay rate of 0.055% per cycle at 1 C over 1000 cycles.

KEYWORDS: Li–S battery, dual-regulation system, mediator, iron phthalocyanine, octafluoronaphthalene



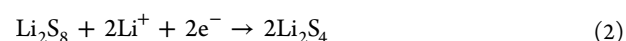
Among state-of-the-art energy storage devices, lithium–sulfur (Li–S) batteries are considered as promising alternatives to lithium-ion batteries (LIBs) owing to their ultrahigh theoretical capacity (1675 mAh g⁻¹) and energy density (2600 Wh kg⁻¹), low cost, and nontoxicity as well as the environmental benignity of sulfur.^{1–3} However, the commercial application of Li–S batteries is impeded by several obstacles, including the insulating nature of sulfur and the corresponding discharge products (Li₂S₂/Li₂S), the shuttle effect of the soluble lithium polysulfides (LiPSs), and the large volume expansion from the reactants to final products, leading to rapid capacity degradation, low Coulombic efficiency, and active material loss.^{4–6} To date, strenuous efforts have been exerted to address the foregoing issues, including the introduction of various sulfur hosts (e.g., heteroatom-doped carbonaceous materials,^{7,8} metal oxides,^{9,10} metal sulfides,^{11,12} and conducting polymers^{13,14}) and a broad range of mediator materials (e.g., metals,¹⁵ metal compounds,¹⁶ and nonmetallic polymer^{17,18}). Despite some success, the performance improvements remain limited, especially at high areal sulfur loadings.^{19,20} More urgently, many scientific and technical issues in the complex conversion reaction system from sulfur to Li₂S, which involves 16 electrons, must be clarified.^{21,22} In

principle, the electrochemical reduction reaction of sulfur can be roughly divided into the following four steps:^{23,24}

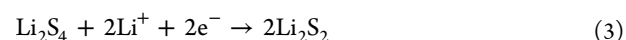
Step I: A solid–liquid conversion from elemental sulfur to soluble Li₂S₈.



Step II: A liquid–liquid reaction between the soluble Li₂S₈ and Li₂S₄.



Step III: A liquid–solid transition from the soluble Li₂S₄ to insoluble Li₂S₂ or Li₂S through the simultaneous reactions in eqs 3 and 4.



Received: April 23, 2020

Accepted: June 3, 2020

Published: June 3, 2020



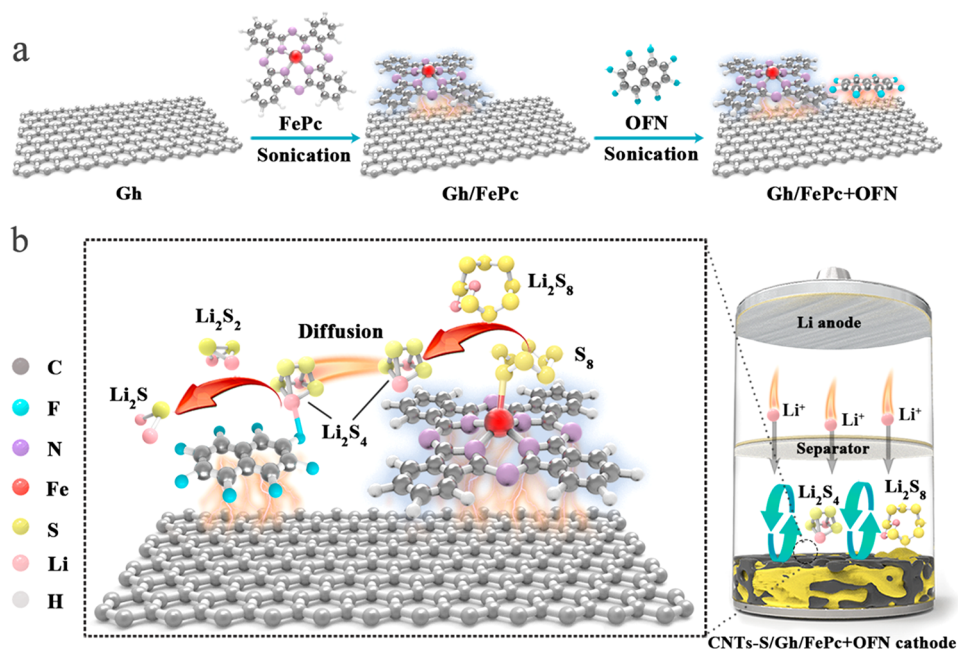
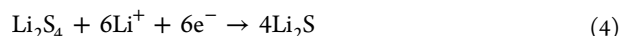


Figure 1. (a) Schematic illustration of the stepwise synthesis process for the Gh/FePc+OFN composites. (b) Schematic configuration of a Li–S battery based on the Gh/FePc+OFN cathode and the mechanisms of adsorption and conversion of LiPSs at the Gh/FePc+OFN composites.



Step IV: A solid–solid reaction between the insoluble Li_2S_2 and Li_2S .



Step II is related to the liquid–liquid transition of soluble LiPSs, and the key issue is how to rapidly slice the LiPSs and effectively inhibit the shuttle effect; thus, this step is understood as the LiPS-scission control step. Lithium supplies become even more important in the liquid–solid (Step III) and solid–solid (Step IV) reactions; thus, Steps III and IV are regarded as Li-supplementation control steps. Recent studies have demonstrated that the Li-supplementation process is a pivotal step because of the sluggish kinetics conversion from Li_2S_4 to the final Li_2S .^{25–27} In this sense, to realize the smooth solid–liquid–solid conversion of sulfur species, the design of an efficient regulation system that can synchronously coordinate the LiPS-scission and Li-supplementation control steps is needed.

Herein, we proposed a dual-regulation strategy and designed a ternary mediator for an advanced Li–S battery by coupling iron phthalocyanine (FePc) and octafluoronaphthalene (OFN) with graphene (Gh) successively, denoted as Gh/FePc+OFN. In our design, FePc acts as the LiPS-scission mediator, which is favorable for facilitating efficient LiPSs conversion, thus mainly accelerating the Step II reaction, whereas OFN favors binding to Li^+ (or LiPSs) *via* Li-bond and serves as an immobilized Li^+ -transfer mediator to accelerate the kinetics of the Step III and Step IV reactions. *In situ* spectroscopy (*i.e.*, Fourier-transform infrared reflection absorption spectroscopy (FT-IRAS), ultraviolet (UV)–visible absorption spectroscopy), *ex situ* X-ray photoelectron spectroscopy (XPS), and electrochemical impedance spectroscopy (EIS) investigations combined with density functional theory (DFT) calculations support and explain our dual-regulation-system model. A cathode integrated with the Gh/FePc+OFN mediator exhibited excellent

performance, delivering an ultrahigh initial capacity of 1604 mAh g^{-1} at 0.2 C (theoretical capacity = 1675 mAh g^{-1}) and exhibiting an ultralow capacity decay rate of 0.055% per cycle at 1 C over 1000 cycles. This dual-regulation strategy can assist in resolving the aforementioned obstacles associated with Li–S batteries, offering a promising avenue to achieve high-capacity Li–S and other rechargeable technologies.

RESULTS AND DISCUSSION

Synthesis and Characterization of Gh/FePc+OFN Composites. The stepwise synthesis of the ternary composite is schematically illustrated in Figure 1a. Initially, FePc molecules were conjugated to the surface of Gh by ultrasonication, producing Gh/FePc composites. To examine the interaction between FePc and Gh, XPS analysis was performed, and the results are presented in Figure S1a. The Fe 2p peaks of the Gh/FePc composites shifted to higher field compared with those of FePc, which is reasonably attributed to the π – π conjugation formed between FePc and Gh.^{28,29} In this noncovalent combination of FePc and Gh, the electrons of the Fe atom in FePc were partially transferred to Gh, resulting in the negative electricity on the surface of Gh.³⁰ The DFT calculation further confirms that the interfacial charge transfer was approximately 0.11e from the FePc molecule to Gh and that intramolecular charge redistribution also occurred at the FePc macrocycle because of the convex structure of FePc (Figure S2). Subsequently, OFN molecules were introduced into the Gh/FePc composites *via* sonication, and the ternary composites thus formed are referred to herein as Gh/FePc+OFN. For comparison, OFN was also mixed with Gh *via* ultrasonication to prepare Gh/OFN composites. Further XPS analysis of the Fe 2p and N 1s spectra of the Gh/FePc and Gh/FePc+OFN composites indicated that the Fe 2p_{1/2} peak at 723.4 eV, Fe 2p_{3/2} peak at 710.8 eV, and N 1s peak at 398.9 eV shifted to higher field after OFN was incorporated into the Gh/FePc composites (Figure S1a,b), whereas the F 1s XPS

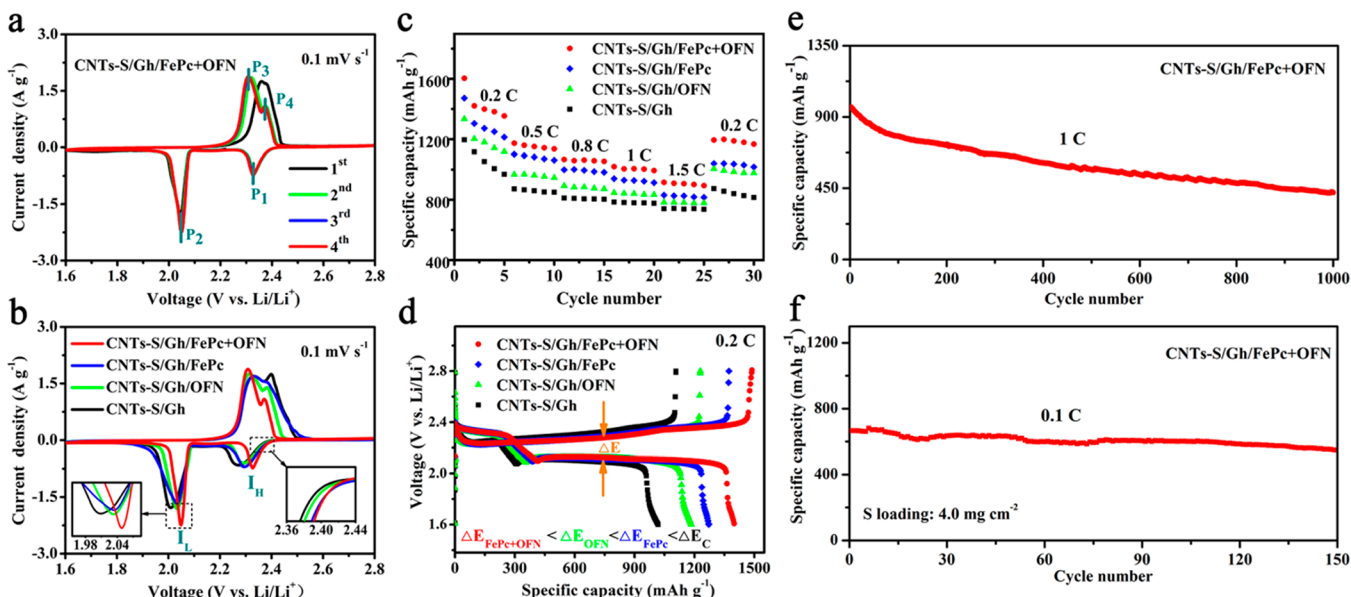


Figure 2. Electrochemical performance of Li-S batteries. (a) CV profiles of CNTs-S/Gh/FePc+OFN cathode between 1.6 and 2.8 V for the first four cycles, recorded at a scan rate of 0.1 mV s^{-1} . (b) The fourth cycle of CV profiles for CNTs-S/Gh, CNTs-S/Gh/OFN, CNTs-S/Gh/FePc, and CNTs-S/Gh/FePc+OFN cathodes. Right inset is higher magnification of the reduction current between 2.36 and 2.44 V, and the left inset is a higher magnification of the reduction current between 1.96 and 2.08 V. (c) The rate capabilities of the CNTs-S/Gh, CNTs-S/Gh/OFN, CNTs-S/Gh/FePc, and CNTs-S/Gh/FePc+OFN cathodes. (d) Galvanostatic charge-discharge profiles of the four cathodes at 0.2 C in the second cycle. (e) Cycling performance of CNTs-S/Gh/FePc+OFN cathode over 1000 cycles at 1 C. (f) Cycling stability of CNTs-S/Gh/FePc+OFN cathode with a sulfur mass loading of 4.0 mg cm^{-2} measured at a rate of 0.1 C for 150 cycles.

spectra of the Gh/OFN and Gh/FePc+OFN composites revealed that the peak at 688.2 eV shifted to a lower field due to the incorporation of FePc (Figure S1c). These findings indicate that Gh/FePc transfers electrons to OFN in the Gh/FePc+OFN system, which can likely be attributed to the excellent electrophilic properties of OFN.³¹ Analyses of the adsorption energies based on the DFT calculation indicated that the most favorable site for OFN molecules on Gh/FePc is next to FePc at the valleys of Gh, as depicted in Figure 1b and Figure S3, resembling the cases of organic molecular self-assembly on inorganic substrates. In addition, the charge transfer from FePc and Gh to OFN was in the range of a few hundredths of electrons per molecule. To investigate the application of the ternary composites in Li-S batteries, Gh/FePc+OFN were incorporated as mediators in carbon nanotubes (CNTs)-S composites to form CNTs-S/Gh/FePc+OFN cathodes. For comparison, CNTs-S/Gh, CNTs-S/Gh/FePc, and CNTs-S/Gh/OFN cathodes were also prepared using the same method, as detailed in the Experimental Section. Li-S batteries were then fabricated and examined to explore the properties of the composites and the sophisticated interactions between LiPSs and composites.

Electrochemical Performance of Li-S Batteries. To evaluate the electrochemical properties of the Li-S battery with the CNTs-S/Gh/FePc+OFN cathode, the cathode was cycled in the voltage range of 1.6–2.8 V at a scan rate of 0.1 mV s^{-1} . Cycle voltammograms (CVs) obtained from the CNTs-S/Gh/FePc+OFN, CNTs-S/Gh/FePc, CNTs-S/Gh/OFN, and CNTs-S/Gh cathodes during the first four cycles are presented in Figure 2a and Figure S4. Two characteristic peaks were observed in the cathodic scans of the four cathodes. The first peak at $\sim 2.3 \text{ V}$ (P_1) is assigned to the conversion of elemental sulfur (S_8) to long-chain LiPSs (Li_2S_n , $4 < n \leq 8$) and further to short-chain LiPSs (Li_2S_n , $n \leq$

4).^{32,33} The second peak at $\sim 2.05 \text{ V}$ (P_2) is assigned to the reduction of the soluble short-chain LiPSs to insoluble Li_2S_2 and eventually to Li_2S .³⁴ During the subsequent anodic scan, Li_2S were transformed into LiPSs and finally into elemental sulfur, giving rise to two distinct oxidation peaks at ~ 2.3 (P_3) and $\sim 2.35 \text{ V}$ (P_4).^{35,36} The variation in the cathodic and anodic peaks between the first and subsequent cycles is attributed to the rearrangement of active sulfur to more energetically stable sites.³⁷ In the subsequent three cycles, the almost identical CV plots for the CNTs-S/Gh/FePc+OFN indicate its highly reversible electrochemical properties. The CV curves of the above four cathodes for the fourth cycle are compared in Figure 2b. The CNTs-S/Gh/FePc+OFN cathode clearly exhibits the highest current density and relatively optimal potential in each redox peak, suggesting that this cathode possess the fastest electrochemical reaction kinetics on the cathode surface. From the right inset of Figure 2b, the onset potentials in the first cathodic peaks for the CNTs-S/Gh/FePc and CNTs-S/Gh/FePc+OFN cathodes are more positive, indicating that the use of the FePc molecule as a mediator can promote the conversion of long-chain LiPSs. In addition, the second cathodic peaks of the CNTs-S/Gh/OFN and CNTs-S/Gh/FePc+OFN cathodes indicate more positive potentials compared with those of the other cathodes without OFN, as observed in the left inset of Figure 2b, suggesting that the OFN mediator plays a crucial role in converting short-chain LiPSs into insulating Li_2S . The voltage hysteresis (ΔV , obtained by subtracting the voltage at P_2 from the voltage at P_3) and collection coefficient (I_L/I_H , the ratio of the peak current at 2.05 V (I_L) associated with the formation of solid sulfides to the peak current at 2.3 V (I_H) associated with the formation of LiPSs) values derived from the CV data in Figure 2b are summarized in Table S1. The CNTs-S/Gh/FePc+OFN cathode exhibit the highest collection coefficient

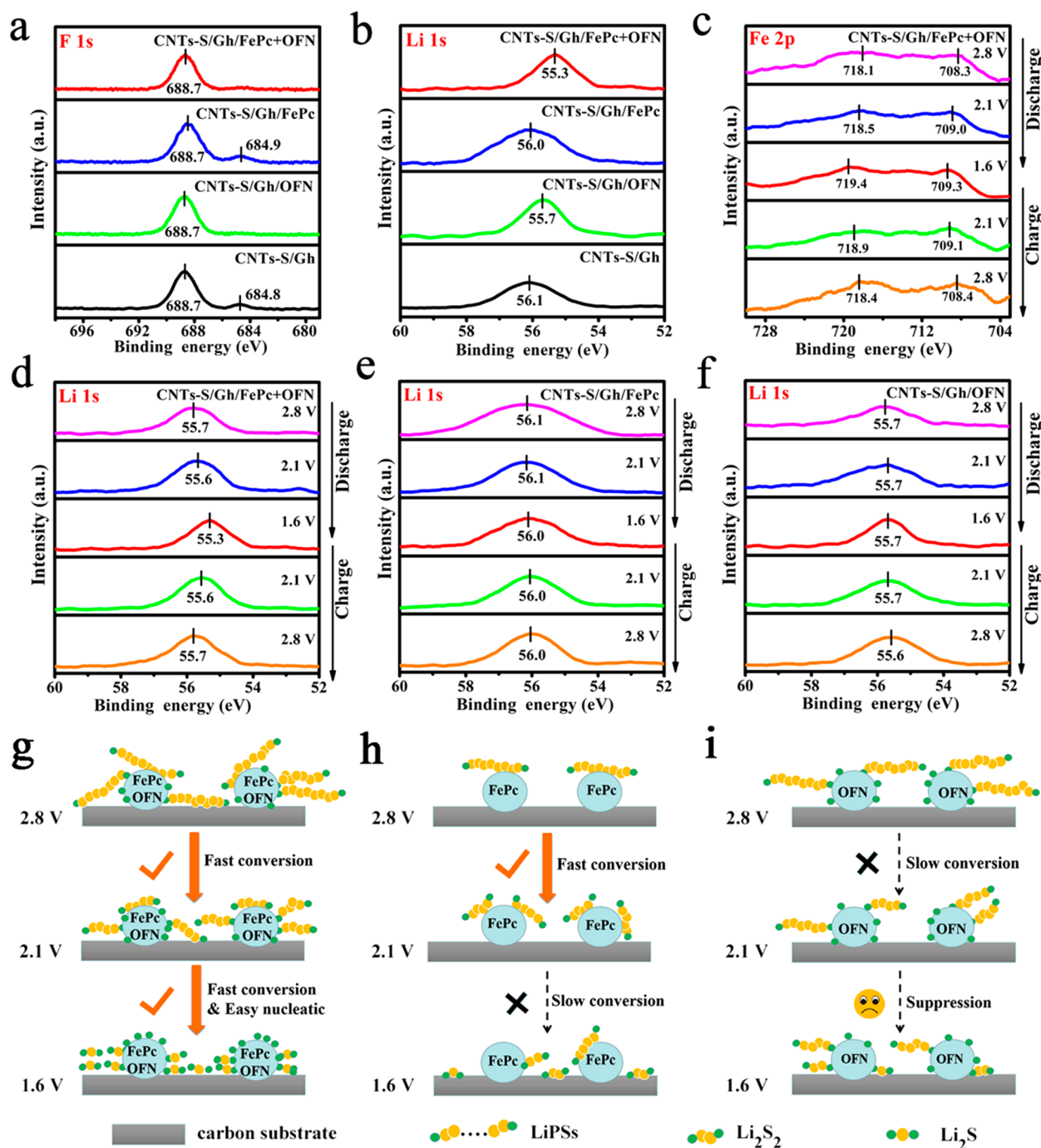


Figure 3. Study of chemical interactions between composites and LiPSs. (a) F 1s, (b) Li 1s XPS spectra of cycled CNTs-S/Gh/FePc+OFN, CNTs-S/Gh/FePc, CNTs-S/Gh/OFN, and CNTs-S/Gh. *Ex situ* XPS spectra of (c) Fe 2p, (d) Li 1s of CNTs-S/Gh/FePc+OFN, (e) Li 1s of CNTs-S/Gh/FePc, (f) Li 1s of CNTs-S/Gh/OFN at five different discharge/charge states: fully charged state at 2.8 V, half discharged state at 2.1 V, fully discharged state at 1.6 V, half charged state at 2.1 V, and fully charged state at 2.8 V. The schematic diagrams to show the adsorption and conversion mechanisms of LiPSs at the surface of (g) CNTs-S/Gh/FePc+OFN, (h) CNTs-S/Gh/FePc, and (i) CNTs-S/Gh/OFN, respectively. The yellow and green balls represent S and Li atoms, respectively.

and the lowest voltage hysteresis, further confirming that the redox reaction kinetics proceed faster on the surfaces of the CNTs-S/Gh cathodes modified with the FePc+OFN mediators.

A series of experiments were carried out to evaluate the effect of the mass ratio of FePc to OFN in Gh/FePc+OFN composites (Figure S5). The results indicate that the battery performance was optimal when the mass ratio of FePc to OFN was chosen as 1:1 in Gh/FePc+OFN composites. The rate

capability of the CNTs-S/Gh/FePc+OFN cathode was compared with those of the other three cathodes at rates from 0.2 to 1.5 C (1 C = 1675 mAh g⁻¹), as shown in Figure 2c. The CNTs-S/Gh/FePc+OFN cathode exhibited the best rate performance, with specific capacities of 1604, 1170, 1067, 1019, and 915 mAh g⁻¹ at 0.2, 0.5, 0.8, 1, and 1.5 C, respectively. In contrast, the initial capacities of the CNTs-S/Gh cathodes with a single mediator, *i.e.*, the CNTs-S/Gh/FePc and CNTs-S/Gh/OFN cathodes, decreased to 1472

and 1334 mAh g⁻¹, respectively. The CNTs-S/Gh cathode without any mediator delivered a limited initial capacity of 1195 mAh g⁻¹ at 0.2 C, and its capacity dramatically decreased to 733 mAh g⁻¹ at a high rate of 1.5 C, indicating its relatively low rate capability. The decline in the capacity of the first several cycles for the four cathodes at 0.2 C may be caused by the rearrangement of active sulfur from its original position to more energetically stable sites during activation process, which is a common phenomenon as it can be found in many previous reports related to Li-S batteries.^{2,35} The highly reversible and excellent rate performance of the CNTs-S/Gh/FePc+OFN cathode was further demonstrated by the easy recovery of the capacity after cycling. As observed in Figure 2c, after cycling at different rates from 0.2 to 1.5 C, the capacity of the CNTs-S/Gh/FePc+OFN cathode was recovered to 1193 mAh g⁻¹ when the current density was abruptly switched back to 0.2 C. Notably, the CNTs-S/Gh/FePc+OFN cathode displayed an ultrahigh initial discharge capacity of 1604 mAh g⁻¹ at 0.2 C, which is quite close to the theoretical value of 1675 mAh g⁻¹ and has rarely been reported previously in the literature (Table S2). The galvanostatic charge/discharge profiles of the four cathodes at a current rate of 0.2 C in the second cycle were compared in Figure 2d. The capacity difference between charge and discharge in Figure 2d is attributed to the aforementioned sulfur rearrangement and the incomplete conversion from long-chain LiPSs to the final solid products at the end of the discharge, which leads to the inevitable loss of active substances in the initial cycles. It was found that the CNTs-S/Gh/FePc+OFN cathode had two well-defined discharge plateaus between 1.6 and 2.8 V (red curves in Figure 2d), which is very well consistent with the multistep electrochemical reaction of sulfur. The contributions of capacities from the reactions between Gh, FePc, and lithium to the battery can be neglected, since these reactions usually occur below 1 V,^{38,39} which are out of probe potentials. In addition, considering the content of OFN in the CNTs-S/Gh/FePc+OFN cathode is as low as 1 wt %, the contribution of OFN to the capacity can also be ignored. Hence, it is reasonable to conclude that sulfur contributes almost all of capacity to the CNTs-S/Gh/FePc+OFN-based battery. The CNTs-S/Gh/FePc+OFN cathode also displayed the lowest voltage hysteresis (ΔE , the voltage gap between the charge and discharge plateaus) among the four cathodes, as shown in Figure 2d and Figures S6 and S7, which is consistent with the ΔV values of the CV plots (Table S1). Because the rate capability is related to the kinetic properties of the Li-S battery, all the above findings strongly indicate that the introduction of FePc+OFN mediator is beneficial for enhancing the sulfur utilization and accelerating the redox kinetics of LiPSs at the cathode surface, resulting in such high-rate performance of the CNTs-S/Gh/FePc+OFN cathode.

The longer cycling life of the Li-S battery using the CNTs-S/Gh/FePc+OFN cathode at 1 C is demonstrated in Figure 2e. The CNTs-S/Gh/FePc+OFN cathode exhibited excellent cycling durability. The discharge capacity remained at 423 mAh g⁻¹ after 1000 cycles *vs* 962 mAh g⁻¹ at the first cycle, indicating a low capacity decay rate of 0.055% per cycle, which is comparable or better than that of other high-energy Li-S batteries (Table S2). Targeting practical applications of Li-S batteries in hybrid electric vehicle (HEV) and electric vehicle (EV) batteries, a CNTs-S/Gh/FePc+OFN cathode with 4.0 mg cm⁻² sulfur areal loading was fabricated and tested. As depicted in Figure 2f, the CNTs-S/Gh/FePc+OFN cathode

displayed a high capacity retention of 83% over 150 cycles, indicating the high performance of the CNTs-S/Gh/FePc+OFN cathode and its potential for practical application.

Mediating Mechanism of Gh/FePc+OFN Mediator in Li-S System. High-resolution F 1s, Li 1s, and Fe 2p XPS spectra of the above four cathodes after two cycles are shown in Figure 3 and Figure S8. Considering the effect of poly(vinylidene fluoride) (PVDF), sodium alginate (C₆H₇O₆Na) was used as a binder instead of PVDF for the F 1s and Li 1s spectra. The peak with a binding energy of 688.7 eV for -CF₃ in the F 1s spectra (Figure 3a), contributed by the complicated decomposition of lithium bis-(trifluoromethanesulfonyl)imide (LiTFSI) in the electrolyte,⁴⁰ appeared in all the samples. However, the peak at approximately 684.8 eV corresponding to LiF products of the decomposition of LiTFSI was not observed for the cathodes containing OFN (CNTs-S/Gh/OFN, CNTs-S/Gh/FePc+OFN) and was only detected in the CNTs-S/Gh and CNTs-S/Gh/FePc spectra, suggesting that OFN might regulate the interface reaction.⁴¹ Additionally, the peaks in the Li 1s spectra of the CNTs-S/Gh/OFN and CNTs-S/Gh/FePc+OFN cathodes were significantly shifted to a lower field compared with those of the CNTs-S/Gh/FePc and CNTs-S/Gh cathodes, as observed in Figure 3b, which is attributed to the electron transfer from the F atom of OFN to Li⁺ (or LiPSs) that results in Li-bond formation, namely, the formation of the Li...F bond, according to previous reports.⁴²⁻⁴⁴ Since the electronegativity of F (3.98) is higher than Li (0.98), a Li-bond (Li...F) can be formed according to Lewis acid-base theory.^{43,44} The F atom in OFN with extra electron pairs, as an electron-rich donor, naturally serves as a Lewis base site and interacts with a strong Lewis acid of terminal Li in LiPSs. The Li-F bond in typical LiF compounds is an ionic bond, which is formed by electrostatic attraction between cations and anions. In addition, the Li atom is the main electron donor in the Li-F ionic bond, whereas it acts as the electron acceptor in the Li-bond (Li...F), resulting in the shift of Li 1s peaks of the CNTs-S/Gh/OFN and CNTs-S/Gh/FePc+OFN to lower binding energy. The newly formed bonds between the F atom of OFN and Li⁺ (or LiPSs) differ from the Li-F ionic bond in typical LiF compounds, which may explain why the LiF peak does not appear in Figure 3a for the cathodes with OFN (CNTs-S/Gh/OFN, CNTs-S/Gh/FePc+OFN). These findings imply that the OFN mediator has a close affinity with Li⁺ (or LiPSs) through the effect of the Li-bond and serves as a Li-supplementation component in the system. Further analysis of the Fe 2p spectra of the CNTs-S/Gh/FePc and CNTs-S/Gh/FePc+OFN cathodes with and without cycling in Figure S8 revealed that the Fe 2p peaks significantly shifted to lower binding energy after cycling. This shift may result from the coordination between the central Fe atom in FePc and the S atom from the LiPSs produced during cycling, where the S atom donates an electron to the Fe atom.⁴⁵⁻⁴⁷ Thus, the central Fe atom exposed in FePc has a high affinity for the S atom of LiPSs and can be regarded as a LiPS-anchor component in the system. The adsorption experiment in Figure S9 further confirms the high affinity and strong anchoring capability of FePc to LiPSs. The Gh was used to improve the conductivity and dispersivity of mediators by forming π - π conjugation with FePc and OFN, which is beneficial to transfer electrons and ions rapidly at the interface and expose more active sites to anchor and transform LiPSs.⁴⁸ *Ex situ* XPS analysis is necessary to better understand the

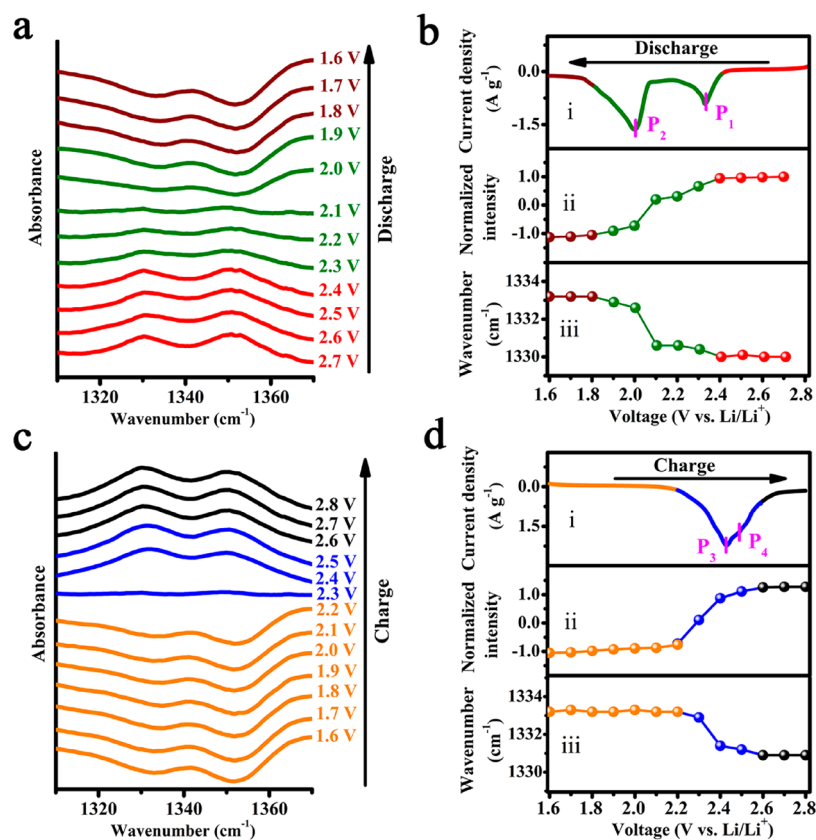


Figure 4. Investigation of the interfacial structures at CNTs-S/Gh/FePc+OFN cathode. *In situ* IR spectra of CNTs-S/Gh/FePc+OFN cathode shown at respective potentials during (a) discharge from 2.8 to 1.6 V and (c) after recharging to 2.8 V. Third (b(i)) discharge and (d(i)) charge electrochemical profiles of the CNTs-S/Gh/FePc+OFN cathode in the IR spectro-electrochemical cell. The scan rate is 0.1 mV s⁻¹. Potential dependence of (b(ii),d(ii)) the normalized peak intensity and (b(iii),d(iii)) wavenumber corresponding to the C–N peak at 1330 cm⁻¹.

surface layer composition of the cathodes at various discharge and charge states.⁴⁹ A series of *ex situ* XPS results for the Fe 2p, N 1s, and Li 1s core level of the CNTs-S/Gh/FePc+OFN cathode surfaces from batteries discharged and charged to different depths (including the fully charged state at 2.8 V, half-discharged state at 2.1 V, fully discharged state at 1.6 V, half-charged state at 2.1 V, and fully charged state at 2.8 V) during the third cycle are presented in Figure 3c,d and Figure S10. As observed in Figure 3c and Figure S10, the Fe 2p and N 1s XPS peaks related to FePc in the CNTs-S/Gh/FePc+OFN cathode gradually shifted to higher binding energy with an increasing degree of discharge, indicating the electron transfers from Fe and N atoms of FePc to the S atom of LiPSs during the discharge process. Upon charging, the shifts in the Fe 2p and N 1s peaks upon discharge were reversed, as observed in Figure 3c and Figure S10, which is indicative of reversible electron transfer from the LiPSs to FePc. Based on the above analysis, we speculate that the FePc mediator catalytic redox reactions of the sulfur cathodes may involve the following mechanism. In the discharge process, long-chain LiPSs adsorbed to FePc absorb electrons from the central Fe atom to form a high-valence Fe, which subsequently promotes the cleavage of the S–S bond in the LiPSs. In the reverse process, the short-chain LiPSs contribute electrons to the central Fe atom of FePc, reducing the high-valence Fe to low-valence Fe, thereby accelerating the oxidation of LiPSs. During periodic changes in the valence state of the central Fe atom, the phthalocyanine ring continuously transfers electrons between

the LiPSs and the catalytic center, emphasizing the important role of the conjugate macrocycle in stabilizing metal ions.⁵⁰ The results above clearly confirm that FePc not only anchors LiPSs *via* a Fe...S coordinate bond but also has a reversible electronic interaction with LiPSs during the charge and discharge process, thus facilitating the conversion of LiPSs and accelerating the kinetic process inside the battery.

Further analysis of the Li 1s spectra of the CNTs-S/Gh/FePc+OFN cathode in Figure 3d revealed that the Li 1s peak shifted to lower binding energy upon discharge and shifted back upon charge, suggesting that there is a strong electron-transfer effect between Li⁺ (or LiPSs) and OFN through the aforementioned Li...F bond in the discharge and charge processes. As comparative experiments, *ex situ* XPS experiments were conducted on CNTs-S/Gh/FePc and CNTs-S/Gh/OFN cathodes. Figure 3e shows that almost no deviation of the Li 1s peak of the CNTs-S/Gh/FePc cathode was detected during charge and discharge, indicating that there is no efficient Li...F bond coordination in the system and reflecting the crucial role of OFN in the formation of Li-bonds. Notably, the Li 1s peak for the CNTs-S/Gh/OFN cathode at each discharge/charge state appeared at lower binding energy than that of the CNTs-S/Gh and CNTs-S/Gh/FePc cathodes (Figure 3f); however, no further peak shift occurred for CNTs-S/Gh/OFN during cycling, implying that the introduction of only OFN into the CNTs-S/Gh cathode hardly cause the variation of Li-bonds during cycling, although it is initially helpful for the formation of the Li...F bond. The

following possible kinetic processes on the CNTs–S/Gh cathode modified by different mediators (FePc+OFN, FePc, OFN) are thus proposed. The FePc mediator possesses a strong capability to capture S in LiPSs through a Fe...S bond and accelerate the kinetics of the LiPS-scission (Step II) reaction. The OFN mediator, however, favors binding to Li⁺ (or LiPSs) via a Li-bond interaction, thereby more efficiently immobilizing the Li⁺ transport for rapid electronic kinetics of the Li-supplementation (Step III and Step IV) reaction. With the advantages from two mediators and their cooperation, the entire sulfur-conversion reaction on the CNTs–S/Gh/FePc+OFN surface is very smooth owing to the considerable acceleration of the kinetics of the LiPS-scission and Li-supplementation reactions, as schematically illustrated in Figure 3g. This finding also provides clues to explain the excellent electrochemical performance of Li–S batteries using CNTs–S/Gh/FePc+OFN cathodes, as shown in Figure 2. For the cathode with only the FePc mediator (CNTs–S/Gh/FePc), LiPS-scission can proceed smoothly upon discharging; however, the subsequent Li-supplementation reaction would be sluggish in the absence of the OFN mediator, as illustrated in Figure 3h. Similarly, when only the OFN mediator is attached on the CNTs–S/Gh cathode, as illustrated in Figure 3i, despite the formation of some Li...F bonds between OFN and Li⁺ (or LiPSs) during charge and discharge, the Li-supplementation reaction is suppressed as the dynamic process of prior LiPS-scission becomes struggling because of the absence of the FePc mediator. Consequently, the overall electrochemical kinetics is limited at the surfaces of the CNTs–S/Gh/FePc and CNTs–S/Gh/OFN cathodes. Overall, by modifying Li-supplementation OFN and LiPS-anchor FePc mediators on a CNTs–S/Gh cathode, a cathode material with a dual-regulation system is proposed that enables the realization of a smooth solid–liquid–solid sulfur conversion reaction.

In situ FT-IRAS experiments were conducted to correlate the electrochemical performance of the CNTs–S/Gh/FePc+OFN cathode in a Li–S battery with the underlying molecular structure mechanism at the cathode surfaces.⁵¹ CV measurements of the IR spectro-electrochemical cell with CNTs–S/Gh/FePc+OFN cathode were also performed. Two pairs of distinct redox peaks were observed in Figure 4b(i),d(i), which are consistent with the standard coin cell, indicating a comparable electrochemical process inside the two cells. The voltage discrepancy between the *in situ* cell and the standard coin cell, which can be attributed to the poor electronic conduction and lithium transport of the IR spectro-electrochemical cell, is not an inherent problem in the design of the IR spectro-electrochemical cell.

The redox processes were monitored by FT-IRAS. Figure 4a,c displays two sets of *in situ* IR spectra for the CNTs–S/Gh/FePc+OFN cathode at different potentials during discharge and charge. The spectrum corresponding to the initial 2.8 V, where no reaction occurs, was taken as a reference, and the spectral variations at subsequent potentials can be attributed to the electrochemical reaction induced by the potential change. Good IR spectra for characteristic C–N stretching vibrations of FePc were obtained between 1310 and 1370 cm^{−1} (Figure 4a,c).^{52,53} To better illustrate the spectroscopic variations within the cathode material during the discharge and charge processes, the intensity and frequency of the 1330 cm^{−1} peak were plotted as a function of the cell potential, as shown in Figure 4b(ii,iii),d(ii,iii). The peak

intensities were normalized by setting the integrated area of the 1330 cm^{−1} peak at 2.7 V to 1. In Figure 4b, it can be clearly observed that during the negative going potential scan, both the intensity and frequency of the C–N peak were almost constant up to 2.4 V; the intensity then started to decrease but the frequency shifted to a higher wavenumber toward 1.8 V; finally, both the intensity and frequency remained constant between 1.8 and 1.6 V. In contrast, when the potential was scanned positively, the spectral features during the charge process were highly reversible, as observed in Figure 4d; the intensity and frequency remained constant until the potential was more positive than 2.2 V, the intensity then increased and reached the original value at approximately 2.6 V while the frequency shifted to lower wavenumber; finally, both the intensity and frequency remained constant with increasing potential for the cathode. The significant changes in the intensity and frequency of the C–N peak during discharge (2.4–1.8 V) and charge (2.2–2.6 V) are very well matched with the electrochemical conversion behavior of sulfur (or lithium sulfide) in the Li–S system, suggesting a strong electronic interaction between sulfur and the FePc molecules during the redox reaction of sulfur on the cathode surface.

Considering the *ex situ* XPS findings, where the N atom in the pyrrole ring of the FePc molecule donates electrons to and accepts electrons from LiPSs through the central Fe atom in the discharge and charge processes, we further investigated the reason for the changes in the C–N peak during discharge and charge as observed in Figure 4. It is generally believed that substances with more sulfur have stronger electron-absorption ability; therefore, it is reasonable to consider the electron absorption ability of LiPSs to be continuously enhanced with increasing the chain length. At the beginning of the discharge (2.7–2.4 V), Li₂S₈, as the main component of the sulfur species in the system, has the strongest electron adsorption capacity to Fe and N atoms of the FePc molecule (the structure of the FePc molecule is delineated in Figure S11) among the LiPSs. Thus, the bond strength of Fe...S was the strongest and the C–N dipole moment or the angle θ between the C–N axis and surface might be the largest at this stage, giving rise to the largest surface normal component of C–N dipoles according to the IR surface dipole selection rule and the weakest bond strength of C–N.⁵⁴ Thus, we observed the strongest intensity and lowest wavenumber of the C–N peak in the IR spectra between 2.7 and 2.4 V in Figure 4b. When the long-chain LiPSs (Li₂S_{*n*}, 4 < *n* ≤ 8) are further reduced to form short-chain LiPSs (Li₂S_{*n*}, *n* ≤ 4) and finally insoluble Li₂S₂/Li₂S in the potential region of 2.4–1.8 V,⁵⁵ the ability of LiPSs to attract electrons from Fe and N atoms become weaker, yielding a stronger C–N bond and leading to a decrease of the surface normal component of C–N dipoles because of the smaller θ or C–N dipole moment. As a result, decreased intensity and an upshift of the C–N peak were observed. At the end of the reduction process (1.8–1.6 V), because the chain length of Li₂S₂/Li₂S varies minimally, less electronic interaction between S and the Fe or N atom occurred in the system, resulting in the constant intensity and frequency of the C–N peak. The opposite trend was observed for the charge process.

In addition to exploring the electrode/electrolyte interface, the change of the electrolyte system is also critical to understanding the mechanism of the Li–S system. *In situ* UV–visible absorption spectroscopy was employed to track the variation of various dissolved LiPS species generated from

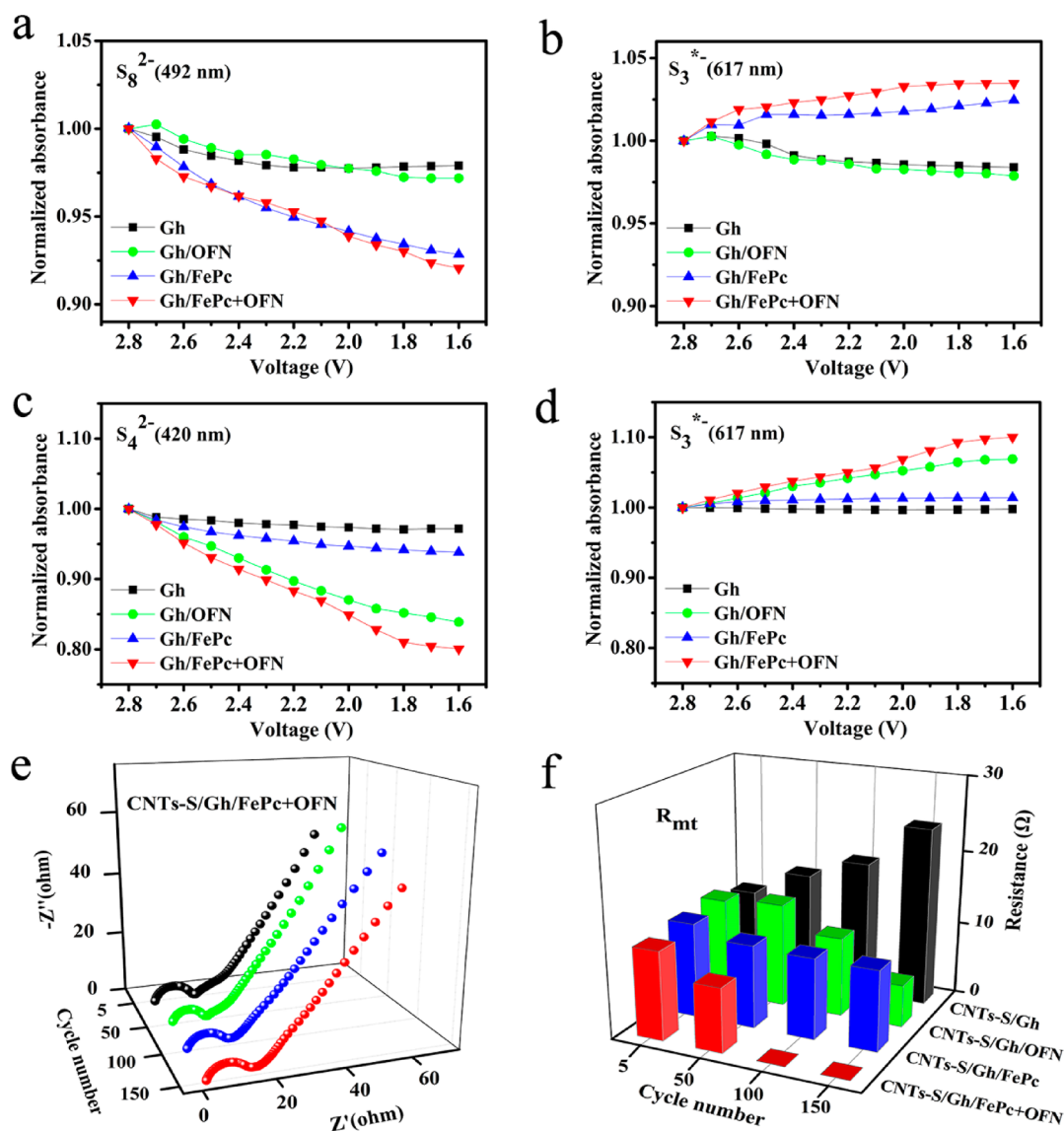


Figure 5. *In situ* UV–visible absorption spectroscopic and EIS study of the catalytic mechanism. The normalized absorbance of (a) S_8^{2-} (492 nm) and (b) S_3^{*-} (617 nm) in Li_2S_8 solution and (c) S_4^{2-} (420 nm), (d) S_3^{*-} (617 nm) in Li_2S_4 solution as a function of potential at different electrodes surfaces during discharge. (e) The Nyquist plots of CNTs–S/Gh/FePc+OFN cathode after 5th, 50th, 100th, and 150th cycles. (f) The mass-transfer resistance (R_{mt}) of four cathodes after different cycles.

the electrochemical reduction of the Li_2S_n ($n = 8, 6, 4$) solution at the four electrodes (Gh/FePc+OFN, Gh/FePc, Gh/OFN, Gh).⁵⁶ The results are presented in Figures S12–S14, where the absorbance peaks at wavelengths of 492, 475, 420, and 617 nm correspond to the S_8^{2-} , S_6^{2-} , S_4^{2-} , and S_3^{*-} ions, respectively.⁵⁷ To clearly demonstrate the changes in the amount of soluble LiPSs during discharge, the normalized intensities of the absorbance peaks for S_8^{2-} (at 492 nm), S_6^{2-} (at 475 nm), S_4^{2-} (at 420 nm), and S_3^{*-} (at 617 nm) in Figures S12–S14 were determined and plotted as a function of potential in Figure 5a–d and Figure S13e,f. It can be observed that in Li_2S_8 solution (Figure 5a,b and Figure S12), the electrodes with the FePc mediator (Gh/FePc and Gh/FePc+OFN) exhibited lower absorbance intensities of S_8^{2-} but higher absorbance intensities of S_3^{*-} than those of the Gh and Gh/OFN electrodes, clearly suggesting that FePc can accelerate the conversion of long-chain LiPSs (S_8^{2-}) and promote the formation of the S_3^{*-} radical. Further analysis revealed that the absorbance intensities of S_8^{2-} and S_3^{*-} for

the Gh/FePc and Gh/FePc+OFN electrodes were almost identical and that those for the Gh and Gh/OFN electrodes were also comparable, hinting that OFN may not affect the conversion of S_8^{2-} . Similar conclusions can also be deduced for fresh Li_2S_6 solution when analyzing the intensities of S_6^{2-} and S_3^{*-} radicals for the above four electrodes, as shown in Figure S13. In contrast, when the four electrodes were exposed to Li_2S_4 solution, the intensities of S_4^{2-} for the two electrodes with OFN, *i.e.*, Gh/FePc+OFN and Gh/OFN, were much lower than those of the two electrodes without OFN, whereas the corresponding intensities of the S_3^{*-} radicals were higher, as observed in Figure 5c,d and Figure S14. This finding indicates that OFN can facilitate the conversion of short-chain LiPSs. In addition, FePc was observed to have a limited catalytic effect on the conversion of S_4^{2-} when the intensities of S_4^{2-} and S_3^{*-} radicals were analyzed for the Gh/FePc electrode. The UV–visible spectroscopy results coupled with the above XPS and FT-IRAS data further confirm that FePc is more inclined to accelerate the conversion of long-chain LiPSs

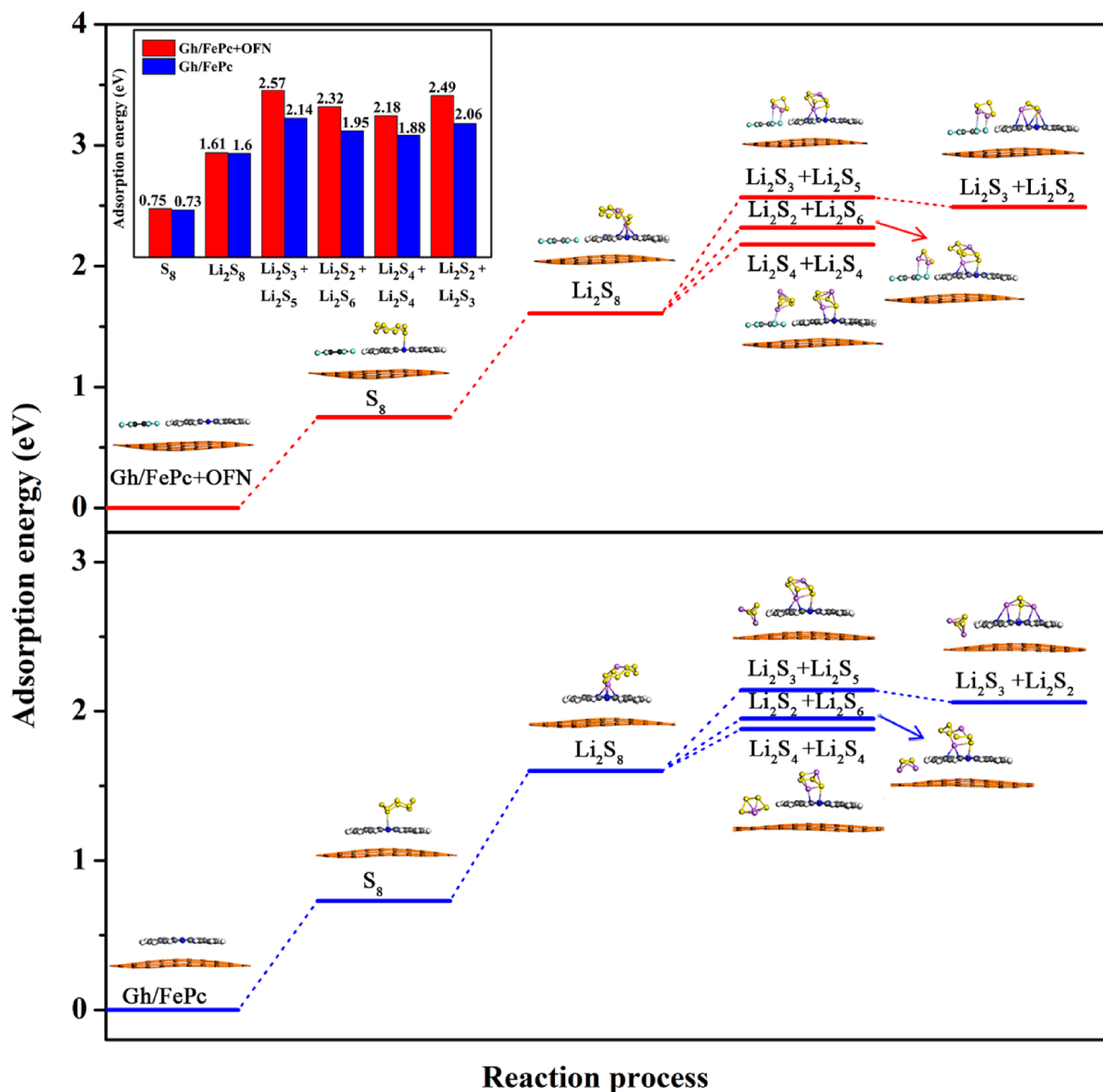


Figure 6. Theoretical analysis of the electrochemical reaction process of LiPSs. The adsorption energies of S_8 and LiPSs deposited onto Gh/FePc+OFN (top) and Gh/FePc (bottom) composites. Inset: Front views of the considered structures of the electrochemical reaction process of LiPSs. The gray, blue, light blue, light purple, cyan, yellow, and white balls represent C, N, Fe, Li, F, S, and H atoms, respectively. Histogram: Comparison of adsorption energy of sulfur species on Gh/FePc and Gh/FePc+OFN composites.

(Li_2S_n , $4 < n \leq 8$) and the generation of $S_3^{* -}$ radicals, whereas OFN is prone to facilitate the conversion of short-chain LiPSs (Li_2S_n , $n \leq 4$).

Considering the strong relationship between the electrochemical performance of Li–S batteries and the interfacial charge-transfer and mass-transfer processes and lithium-ion diffusion in the cathode materials, EIS measurements were performed for the four cathodes after cycling for different cycles at 1 C.^{58,59} To better analyze the EIS results, the electrolyte resistance (R_e), charge-transfer resistance (R_{ct}), and mass-transfer resistance (R_{mt}) parameters were determined by calculating each impedance spectrum in Figure 5e and Figure S15 with the corresponding equivalent circuits,^{60,61} and presented in Table S3. As observed in Table S3, the R_e and

R_{ct} values for the four cathodes showed little fluctuation over the span of 5–150 cycles owing to the efficient electronic/ionic transport between the cathode material and electrolyte. Unlike for R_e and R_{ct} , there was a significant increase in R_{mt} at the interface in the CNTs–S/Gh cathode from the 5th to 150th cycle, as clearly observed in Figure 5f, which is attributed to the dramatically destructive effect of the incomplete evolution and consequent uncontrollable accumulation of discharge products (Li_2S_2/Li_2S). However, the R_{mt} values of the cathodes with the incorporation of OFN (CNTs–S/Gh/OFN and CNTs–S/Gh/FePc+OFN cathodes) decreased more with increasing cycle number than those of the CNTs–S/Gh/FePc cathode. In particular, the lowest R_{mt} of the CNTs–S/Gh/FePc+OFN cathodes in all the measured

cycles indicates the favorable and sustainable mass-transfer and regulating effect on the deposition of discharge products at the interface. It is apparent that OFN can greatly enhance the reaction kinetics of conversion from short-chain LiPSs to insulating $\text{Li}_2\text{S}_2/\text{Li}_2\text{S}$, which corresponds well to the *in situ* spectroscopic results and the superior electrochemical performance of the CNTs-S/Gh/FePc+OFN-based Li-S battery.

The XPS, FT-IRAS, and UV-visible spectroscopy and EIS measurements strongly confirm that FePc acts as an efficient anchor and scissor for LiPSs through Fe...S coordination to mainly facilitate the liquid-liquid transformation of LiPSs, whereas OFN enables Li-bond interaction with LiPSs and accelerates the kinetics of the liquid-solid nucleation and growth of Li_2S .

With the help of DFT calculations, the detailed reaction process of LiPSs on the Gh/FePc+OFN and Gh/FePc was further analyzed, as shown in Figure 6. The adsorption ability of Gh/FePc to long-chain sulfur species (S_8 and Li_2S_8) was equivalent to that of Gh/FePc+OFN; however, higher adsorption energies were generated on Gh/FePc+OFN when Li_2S_8 is split into short-chain sulfur species (Li_2S_4 , Li_2S_3 , Li_2S_2). This phenomenon is attributed to the difference in the adsorption behavior of short-chain sulfur species on the surfaces of Gh and OFN, which ultimately affects the reaction process of sulfur species on Gh/FePc and Gh/FePc+OFN. Although FePc exhibits high adsorption ability for LiPSs, the low adsorptivity of Gh limits the conversion of LiPSs on its surface, and a long diffusion path from the FePc surface to the nearby Gh substrate was formed before conversion occurred. This diffusion process was much slower than the electrochemical reaction, greatly reducing the trapping efficiency and utilization of the LiPSs. In contrast, OFN in the dual-regulation system served as a moderate acceptor, enabling the fast nucleation and conversion of LiPSs on its surface, and the chemical/physical binding of LiPSs on its surface was much stronger than that on bare Gh. As illustrated, the LiPSs trapped on the FePc surface rapidly diffused to the edge of OFN, forming Li...F bonds and were then converted into insoluble Li_2S_3 . The short-range diffusion of short-chain Li_2S_n ($n \leq 4$) from FePc to OFN boosted the efficiency through fast trapping and conversion. Thus, fast nucleation/conversion of the LiPSs was realized in an ideal manner at the interface; as a result, the LiPSs shuttling was effectively restrained and, more importantly, sulfur utilization was noticeably improved.

CONCLUSIONS

The crucial role of the Gh/FePc+OFN mediator in the electrochemical kinetics at the cathode surfaces of Li-S batteries was investigated using multiple *in situ* spectroscopy techniques and *ex situ* XPS as well as DFT computations. This Gh/FePc+OFN mediator serves as a dual-regulation system in the reaction kinetics of LiPSs in Li-S batteries. FePc, with its strong adsorbing and catalysis ability of LiPSs, mainly promotes the conversion of long-chain LiPSs (Step II), whereas OFN enriches the Li^+ via Li-bonds and serves as an immobilized Li^+ -transfer mediator, accelerating the kinetics of the conversion of short-chain LiPSs (Step III and Step IV). Li-S batteries incorporating the dual regulation system, *i.e.*, Gh/FePc+OFN mediator, into the cathode exhibited extraordinary electrochemical performance, with an ultrahigh initial capacity of 1604 mAh g^{-1} and a decay rate as low as 0.055% per cycle at 1 C over 1000 cycles, which is far superior to the

performance of other reported Li-S batteries. The design of Gh/FePc+OFN mediator with a dual-regulation function is clearly critical for the sulfur conversion reaction and has an enormous potential for the application of Li-S batteries for EVs and renewable energy storage. We believe that this dual-regulation strategy can also be further extended to the design of other electrode materials for advanced energy storage.

EXPERIMENTAL SECTION

Synthesis of CNTs-S/Gh/FePc+OFN, CNTs-S/Gh/FePc, CNTs-S/Gh/OFN, CNTs-S/Gh. Before synthesis of CNTs-S/Gh/FePc+OFN cathodes, CNTs-S composites were prepared with a melting-diffusion treatment, in which the sulfur powders (>99.99%, metal basis, Aladdin) and the commercial multiwalled CNTs (>95%, inside diameter, 3–5 nm; Aladdin) were mixed in carbon disulfide (CS_2 , >99.9%; Aladdin) solution at a mass ratio of 4:1, followed by heating at 155 °C overnight. The sulfur contents of CNTs-S composites in this work were usually controlled between 75–80 wt %. Gh/FePc+OFN composites were fabricated by dispersing Gh, FePc (>98%, Alfa Aesar) and OFN (>98%, Alfa Aesar) into 1-methyl-2-pyrrolidone (NMP, >99.9%, Aladdin) solution according to a mass ratio of 1:1:1 and then the mixture was treated through ultrasonication and dried at 55 °C for 12 h. Subsequently, the mixtures of 80 wt % CNTs-S powders, 12 wt % conductive scaffold, 5 wt % PVDF, and 3 wt % Gh/FePc+OFN were added in NMP under vigorous stirring for 2 h to form a homogeneous suspension. In order to produce CNTs-S/Gh/FePc+OFN cathodes, the obtained suspensions were cast on an aluminum foil for electrochemical performance measurements or a carbon paper for FT-IRAS measurements and were allowed to evaporate at 55 °C in vacuum for 24 h. The sulfur mass loading in the cathodes is $\sim 1.2 \text{ mg cm}^{-2}$. The dried cathode was punched into a disk of 14 mm in diameter for assembling cells. CNTs-S/Gh/FePc, CNTs-S/Gh/OFN, and CNTs-S/Gh cathodes were prepared by the similar operations, only replacing Gh/FePc+OFN by Gh/FePc, Gh/OFN, or Gh.

Electrochemical Measurements. The coin-type (CR2025) cells were assembled in an argon-filled glovebox with water and oxygen below 0.1 ppm. Lithium metal was employed as the anode. 1.0 M LiTFSI in 1,3-dioxolane (DOL)/1,2-dimethoxyethane (DME) (DOL/DME, 1:1 in volume, Suzhou DodoChem Ltd.) containing 0.2 wt % LiNO_3 additive was used as the electrolyte. The electrolyte/sulfur ratio for the coin cell was about 15:1 ($\mu\text{L}/\text{mg}$), and both the areas of cathode and anode are approximately 1.53 cm^2 . A Celgard 2400 porous separator was sandwiched between the anode and cathode. Considering the reproducibility of the experiment, 10 cells were prepared and tested in this work under the same operating conditions. Cyclic voltammetry and EIS were characterized by a CHI760E electrochemical workstation (CH Instruments). The CV was recorded with a scan rate of 0.1 mV s^{-1} between 1.6 and 2.8 V (*vs* Li/Li⁺). EIS was performed on the AC amplitude of 5 mV in the frequency range from 100 kHz to 0.01 mHz under open-circuit voltage and room temperature conditions. Galvanostatic charge-discharge curves, rate performance, and cycle life curves at 1 C were tested by a Neware Battery Testing System (Shen Zhen Netware Technology) within the potential range of 1.6–2.8 V (*vs* Li/Li⁺) at room temperature. The current and capacity were calculated on the basis of the mass of the sulfur element.

XPS Characterization. XPS experiments were taken with a Thermo Fisher Scientific K-Alpha spectrometer using a monochromatic Al-K α X-ray as an excitation (10 mA, 15 kV). The analysis area was around 500 μm in diameter, and the instrument base pressure was 2×10^{-9} mbar. Binding energy scale was calibrated to the C 1s peak at around 284.8 eV. To determine the surface chemical states of the cathodes developed under cycling of Li-S batteries, the samples for *ex situ* XPS measurements were prepared by discharging (or recharging) the cathode to certain discharge (or charge) states, disassembled in the argon-filled glovebox, and sealed in a vial before being quickly transferred to the XPS chamber.

Electrochemical *In Situ* FT-IRAS Measurements. The Thermo Fisher iS50 Fourier-transform infrared reflection spectrometer employed in this work was equipped with a liquid-nitrogen-cooled wide-band mercury, cadmium, telluride (MCT) detector. The configuration of the spectro-electrochemical cell is shown in Figure S16. Prior to use, the cell was ultrasonically cleaned in absolute ethanol and dried with nitrogen gas. Li foil and a porous Celgard 2400 membrane were used as the anode and separator, respectively. A 14 mm diameter carbon paper coated with CNTs–S/Gh/FePc+OFN was employed as the cathode and was mounted onto a micrometer screw in the spectro-electrochemical cell. The cell was assembled with the electrolyte of 1.0 M LiTFSI dissolved in a binary solvent of DOL and DME (DOL/DME, 1:1 in volume) with 0.2 wt % LiNO₃ additive in the glovebox. The electrical conduction of the cathode and anode were achieved by a Ti wire and the stainless-steel micrometer screw. A *p*-polarized IR beam was incident onto the cathode/electrolyte interface by passing through the optical diamond window with an angle of 45°, and then it was reflected by the cathode surface. In order to avoid the strong IR absorption by organic electrolyte, the cathode was precisely pushed down to the triangular diamond window to form a thin solution layer (1–2 μm). According to the Lambert–Beer law, the attenuation of IR light before reaching the electrode surface by passing through the thin electrolyte layer with an angle at 45° was estimated as ~0.7. It is worthwhile noting that, before IR data collection, the cathode was cycled at 0.1 mV s⁻¹ between 1.6 and 2.8 V until a stable voltammogram was obtained. The IR measurements were carried out with a scanning potential mode. Each IR spectra was acquired at cathode surface with an accumulation time of 10 s while potential was scanned with a rate of 0.1 mV s⁻¹. A CHI760E electrochemical workstation (CH Instruments) was used for potential control during the experiments. The current densities were referred to the geometric area of the cathode (approximately 1.53 cm⁻²). A reference single-beam spectrum *R*₀ was obtained at the first 2.8 V, and then single-beam spectra *R* were recorded at 0.1 V intervals at sampling potentials between 2.7 and 1.6 V. At each potential, 10 scans were taken at 0.5 cm⁻¹ resolution and normalized to the reference spectrum to give the resulting absorbance spectra *A* = -log(*R*/*R*₀). By this normalization, the positive peaks in the resulting spectra indicate a gain of the corresponding products, while negative peaks indicate losses of reactants.

Electrochemical *In Situ* UV–Visible Absorption Spectroscopy Measurements. The two-electrode spectroscopic cell was prepared using Gh/FePc+OFN modified glassy carbon (GC) as the cathode, Ti wire as the anode, and 0.5 mM L⁻¹ Li₂S_{*n*} (*n* = 8, 6, 4) electrolyte, as described in our previous work.^{41,55} The LiPS solutions (Li₂S₈, Li₂S₆, Li₂S₄) were prepared by mixing Li₂S and S₈ powder with the stoichiometric molar ratio (1:7 for Li₂S₈, 1:5 for Li₂S₆, and 1:3 for Li₂S₄) into DMSO. After stirring for 24 h at room temperature (~25 °C) in an argon atmosphere, the cell was assembled in an argon-filled glovebox and sealed with low vapor-pressure epoxy. For the *in situ* UV–visible absorption spectroscopic measurements, the cell was attached to a UV–visible spectrometer (UV-1800, Malvern Panalytical); in this way, the UV beam can directly focus on the glass of the cell. UV–visible spectra were recorded over the range of 200–800 nm with a potential interval of 0.1 mV during discharge. The potential was controlled using an electrochemical workstation (CHI760E, CH Instruments). Here, the UV–visible absorbance was normalized by making the absorbance at 2.8 V as 1. For comparison, the Gh/FePc, Gh/OFN, and Gh composites modified GC electrodes were also measured with the same method.

Computational Methods. Spin-polarized DFT calculations were performed using the FHI-aims code engaging the Perdew, Burke, and Ernzerhof (PBE) exchange correlation functional.^{62–64} The electron density was determined through iterative diagonalization of the Kohn–Sham Hamiltonian by Pulay mixing. The *tight* default basis set was employed for all considered atoms (H, Li, C, N, F, Fe, S). To account for the weak noncovalent intermolecular interaction, these functionals were augmented by the van der Waals scheme of Tkatchenko and Scheffler.⁶⁵ The hybrid system was modeled by a periodic 2-dimensional graphene substrate with molecules and LiPS

adsorbates. The hexagonal supercell (10 × 10, *a* = *b* = 24.5 Å) containing 200 carbon atoms was chosen for Gh. A vacuum region of 30 Å was introduced to ensure the energy convergence. In the self-assembled molecular layer, Gh substrate and LiPSs adsorbates were all relaxed until the residual force components were adjusted below 0.01 eV Å⁻¹. A (3 × 3 × 1) Monkhorst–Pack mesh of *k*-points was adopted to sample the Brillouin zone. Gaussian smearing was used with a width of 0.05 eV to determine the partial occupancies. Moreover, the electron transfers between the organic molecules and Gh at the optimal configurations were carried out by the Mulliken population as it provided trends in agreement to more sophisticated NBO approaches.⁶⁶ To evaluate the interaction between the adsorbate and the Gh substrate, the adsorption energy was calculated following the equation,

$$\Delta E_{\text{ad}} = nE_{\text{molecule}} + E_{\text{Gh}} - E_{\text{molecule+Gh}} \quad (6)$$

in which $E_{\text{molecule+Gh}}$ is the total energy of the hybrid organic–inorganic system, E_{molecule} and E_{Gh} are the total energies of the separated organic molecules and Gh, respectively, and *n* is the number of molecules deposited onto the substrate.

ASSOCIATED CONTENT

Supporting Information

The Supporting Information is available free of charge at <https://pubs.acs.org/doi/10.1021/acsnano.0c03403>.

XPS spectra of FePc, Gh/FePc, and Gh/FePc+OFN composites; theoretical analysis of the adsorption structures of Gh/FePc and Gh/FePc+OFN by DFT calculations; CVs of CNTs–S/Gh, CNTs–S/Gh/OFN, CNTs–S/Gh/FePc, and CNTs–S/Gh/FePc+OFN cathodes; comparison of voltage hysteresis and collection coefficient of the four cathodes; rate performances of CNTs–S/Gh/FePc+OFN cathodes with different mass ratios of FePc to OFN in Gh/FePc+OFN composites; comparison of voltage hysteresis of the four cathodes obtained from the galvanostatic charge–discharge profiles at 0.2 C; galvanostatic discharge–charge plots of CNTs–S/Gh/FePc+OFN cathodes in different rates; characteristics of various composites reported in literatures; XPS spectra of CNTs–S/Gh/FePc and CNTs–S/Gh/FePc+OFN cathodes with cycling and without cycling; LiPS adsorption tests of Gh, Gh/OFN, Gh/FePc, and Gh/FePc+OFN composites; *ex situ* XPS spectra of N 1s of CNTs–S/Gh/FePc+OFN cathode; molecular structure of iron phthalocyanine; *in situ* UV–visible absorption spectra of Gh, Gh/OFN, Gh/FePc, and Gh/FePc+OFN electrodes in Li₂S_{*n*} (*n* = 8, 6, 4) solution; Nyquist plots and the electrolyte resistance (*R*_e), charge-transfer resistance (*R*_{ct}), and the mass-transfer resistance (*R*_{mt}) of the four cathodes after different cycles; and structure of IR spectro-electrochemical cell (PDF)

AUTHOR INFORMATION

Corresponding Author

Zhi Yang – Key Laboratory of Carbon Materials of Zhejiang Province, Wenzhou University, Wenzhou 325035, China;
orcid.org/0000-0002-9265-5041; Email: yang201079@126.com

Authors

Suya Zhou – Key Laboratory of Carbon Materials of Zhejiang Province, Wenzhou University, Wenzhou 325035, China

Shuo Yang – Key Laboratory of Carbon Materials of Zhejiang Province and College of Electrical and Electronic Engineering, Wenzhou University, Wenzhou 325035, China

Xinwei Ding – Key Laboratory of Carbon Materials of Zhejiang Province, Wenzhou University, Wenzhou 325035, China

Yuchong Lai – Key Laboratory of Carbon Materials of Zhejiang Province, Wenzhou University, Wenzhou 325035, China

Huagui Nie – Key Laboratory of Carbon Materials of Zhejiang Province, Wenzhou University, Wenzhou 325035, China

Yonggui Zhang – Key Laboratory of Carbon Materials of Zhejiang Province, Wenzhou University, Wenzhou 325035, China

Dan Chan – Key Laboratory of Carbon Materials of Zhejiang Province, Wenzhou University, Wenzhou 325035, China

Huan Duan – School of Chemistry and Chemical Engineering, Southwest University, Chongqing 400715, China

Shaoming Huang – School of Materials and Energy, Guangdong University of Technology, Guangzhou 510006, China; orcid.org/0000-0003-0242-1143

Complete contact information is available at:
<https://pubs.acs.org/10.1021/acsnano.0c03403>

Author Contributions

#S.Z. and S.Y. contributed equally to this work.

Notes

The authors declare no competing financial interest.

ACKNOWLEDGMENTS

The work was supported in part by grants from the National Natural Science Foundation of China (Grants 51972238, 21875166, and 51920105004), Natural Science Foundation of Zhejiang Province (Grants LR18E020001 and LQ19B030006), and General Research Foundation of Zhejiang Educational Committee (Grant Y201839009), and Science and Technology Project of Zhejiang Province (Grant LGF18B050005). We are grateful to Chongqing Qindong Tech. Co. Ltd. for scientific computing assistance.

REFERENCES

- (1) Li, G.; Wang, X.; Seo, M. H.; Li, M.; Ma, L.; Yuan, Y.; Wu, T.; Yu, A.; Wang, S.; Lu, J.; Chen, Z. Chemisorption of Polysulfides through Redox Reactions with Organic Molecules for Lithium-Sulfur Batteries. *Nat. Commun.* **2018**, *9*, 705.
- (2) Li, J.; Chen, C.; Chen, Y.; Li, Z.; Xie, W.; Zhang, X.; Shao, M.; Wei, M. Polysulfide Confinement and Highly Efficient Conversion on Hierarchical Mesoporous Carbon Nanosheets for Li-S Batteries. *Adv. Energy Mater.* **2019**, *9*, 1901935.
- (3) Shin, W.; Lu, J.; Ji, X. ZnS Coating of Cathode Facilitates Lean-Electrolyte Li-S Batteries. *Carbon Energy* **2019**, *1*, 165–172.
- (4) Lin, H.; Yang, L.; Jiang, X.; Li, G.; Zhang, T.; Yao, Q.; Zheng, G. W.; Lee, J. Y. Electrocatalysis of Polysulfide Conversion by Sulfur-Deficient MoS₂ Nanoflakes for Lithium-Sulfur Batteries. *Energy Environ. Sci.* **2017**, *10*, 1476–1486.
- (5) Chen, W.; Lei, T.; Lv, W.; Hu, Y.; Yan, Y.; Jiao, Y.; He, W.; Li, Z.; Yan, C.; Xiong, J. Atomic Interlamellar Ion Path in High Sulfur Content Lithium-Montmorillonite Host Enables High-Rate and Stable Lithium-Sulfur Battery. *Adv. Mater.* **2018**, *30*, No. 1804084.
- (6) Shi, H.; Lv, W.; Zhang, C.; Wang, D.; Ling, G.; He, Y.; Kang, F.; Yang, Q. Functional Carbons Remedy the Shuttling of Polysulfides in Lithium-Sulfur Batteries: Confining, Trapping, Blocking, and Breaking Up. *Adv. Funct. Mater.* **2018**, *28*, 1800508.
- (7) Zhou, W.; Wang, C.; Zhang, Q.; Abruña, H. D.; He, Y.; Wang, J.; Mao, S. X.; Xiao, X. Tailoring Pore Size of Nitrogen-Doped Hollow

Carbon Nanospheres for Confining Sulfur in Lithium-Sulfur Batteries. *Adv. Energy Mater.* **2015**, *5*, 1401752.

(8) Song, J.; Gordin, M. L.; Xu, T.; Chen, S.; Yu, Z.; Sohn, H.; Lu, J.; Ren, Y.; Duan, Y.; Wang, D. Strong Lithium Polysulfide Chemisorption on Electroactive Sites of Nitrogen-Doped Carbon Composites for High-Performance Lithium-Sulfur Battery Cathodes. *Angew. Chem., Int. Ed.* **2015**, *54*, 4325–4329.

(9) Li, Z.; Zhang, J.; Lou, X. W. D. Hollow Carbon Nanofibers Filled with MnO₂ Nanosheets As Efficient Sulfur Hosts for Lithium-Sulfur Batteries. *Angew. Chem., Int. Ed.* **2015**, *54*, 12886–12890.

(10) Liang, X.; Kwok, C. Y.; Lodi-Marzano, F.; Pang, Q.; Cuisinier, M.; Huang, H.; Hart, C. J.; Houtarde, D.; Kaup, K.; Sommer, H.; Brezesinski, T.; Janek, J.; Nazar, L. F. Tuning Transition Metal Oxide-Sulfur Interactions for Long Life Lithium Sulfur Batteries: The “Goldilocks” Principle. *Adv. Energy Mater.* **2016**, *6*, 1501636.

(11) Lei, T.; Chen, W.; Huang, J.; Yan, C.; Sun, H.; Wang, C.; Zhang, W.; Li, Y.; Xiong, J. Multi-Functional Layered WS₂ Nanosheets for Enhancing the Performance of Lithium-Sulfur Batteries. *Adv. Energy Mater.* **2017**, *7*, 1601843.

(12) Tang, W.; Chen, Z.; Tian, B.; Lee, H. W.; Zhao, X.; Fan, X.; Fan, Y.; Leng, K.; Peng, C.; Kim, M. H.; Li, M.; Lin, M.; Su, J.; Chen, J.; Jeong, H. Y.; Yin, X.; Zhang, Q.; Zhou, W.; Loh, K. P.; Zheng, G. W. *In Situ* Observation and Electrochemical Study of Encapsulated Sulfur Nanoparticles by MoS₂ Flakes. *J. Am. Chem. Soc.* **2017**, *139*, 10133–10141.

(13) Li, W.; Zhang, Q.; Zheng, G.; Seh, Z. W.; Yao, H.; Cui, Y. Understanding the Role of Different Conductive Polymers in Improving the Nanostructured Sulfur Cathode Performance. *Nano Lett.* **2013**, *13*, 5534–5540.

(14) Wang, X.; Yang, C.; Xiong, X.; Chen, G.; Huang, M.; Wang, J. H.; Liu, Y.; Liu, M.; Huang, K. A Robust Sulfur Host with Dual Lithium Polysulfide Immobilization Mechanism for Long Cycle Life and High Capacity Li-S Batteries. *Energy Storage Mater.* **2019**, *16*, 344–353.

(15) Li, Y.; Fan, J.; Zheng, M.; Dong, Q. A Novel Synergistic Composite with Multi-Functional Effects for High-Performance Li-S Batteries. *Energy Environ. Sci.* **2016**, *9*, 1998–2004.

(16) Cheng, Z.; Xiao, Z.; Pan, H.; Wang, S.; Wang, R. Elastic Sandwich-Type rGO-VS₂/S Composites with High Tap Density: Structural and Chemical Cooperativity Enabling Lithium-Sulfur Batteries with High Energy Density. *Adv. Energy Mater.* **2018**, *8*, 1702337.

(17) Chen, C.; Peng, H.; Hou, T.; Zhai, P.; Li, B.; Tang, C.; Zhu, W.; Huang, J.; Zhang, Q. A Quinonoid-Imine-Enriched Nanostructured Polymer Mediator for Lithium-Sulfur Batteries. *Adv. Mater.* **2017**, *29*, 1606802.

(18) Gerber, L. C. H.; Frischmann, P. D.; Fan, F. Y.; Doris, S. E.; Qu, X.; Scheuermann, A. M.; Persson, K.; Chiang, Y. M.; Helms, B. A. Three-Dimensional Growth of Li₂S in Lithium-Sulfur Batteries Promoted by a Redox Mediator. *Nano Lett.* **2016**, *16*, 549–554.

(19) Peng, H.; Huang, J.; Cheng, X.; Zhang, Q. Review on High-Loading and High-Energy Lithium-Sulfur Batteries. *Adv. Energy Mater.* **2017**, *7*, 1700260.

(20) Fan, Y.; Yang, Z.; Hua, W.; Liu, D.; Tao, T.; Rahman, M. M.; Lei, W.; Huang, S.; Chen, Y. Functionalized Boron Nitride Nanosheets/Graphene Interlayer for Fast and Long-Life Lithium-Sulfur Batteries. *Adv. Energy Mater.* **2017**, *7*, 1602380.

(21) Yin, Y.; Xin, S.; Guo, Y.; Wan, L. Lithium-Sulfur Batteries: Electrochemistry, Materials, and Prospects. *Angew. Chem., Int. Ed.* **2013**, *52*, 13186–13200.

(22) Li, M.; Bai, Z.; Li, Y.; Ma, L.; Dai, A.; Wang, X.; Luo, D.; Wu, T.; Liu, P.; Yang, L.; Amine, K.; Chen, Z.; Lu, J. Electrochemically Primed Functional Redox Mediator Generator from the Decomposition of Solid State Electrolyte. *Nat. Commun.* **2019**, *10*, 1890.

(23) Zhang, S. S. Role of LiNO₃ in Rechargeable Lithium/Sulfur Battery. *Electrochim. Acta* **2012**, *70*, 344–348.

(24) Walus, S.; Barchasz, C.; Colin, J. F.; Martin, J. F.; Elkaim, E.; Lepretre, J. C.; Allain, F. New Insight into the Working Mechanism of

Lithium-Sulfur Batteries: *In Situ* and Operando X-ray Diffraction Characterization. *Chem. Commun.* **2013**, *49*, 7899–7901.

(25) Ye, H.; Sun, J.; Zhang, S.; Lin, H.; Zhang, T.; Yao, Q.; Lee, J. Y. Stepwise Electrocatalysis As a Strategy against Polysulfide Shuttling in Li-S Batteries. *ACS Nano* **2019**, *13*, 14208–14216.

(26) Zhang, L.; Chen, X.; Wan, F.; Niu, Z.; Wang, Y.; Zhang, Q.; Chen, J. Enhanced Electrochemical Kinetics and Polysulfide Traps of Indium Nitride for Highly Stable Lithium-Sulfur Batteries. *ACS Nano* **2018**, *12*, 9578–9586.

(27) Yan, Y.; Cheng, C.; Zhang, L.; Li, Y.; Lu, J. Deciphering the Reaction Mechanism of Lithium-Sulfur Batteries by *In Situ/Operando* Synchrotron-Based Characterization Techniques. *Adv. Energy Mater.* **2019**, *9*, 1900148.

(28) Zhang, Y.; Xu, C.; Li, B. Self-Assembly of Hemin on Carbon Nanotube As Highly Active Peroxidase Mimetic and Its Application for Biosensing. *RSC Adv.* **2013**, *3*, 6044–6050.

(29) Cárdenas-Jirón, G. I.; León-Plata, P.; Cortes-Arriagada, D.; Seminario, J. M. Electron Transport Properties through Graphene Oxide-Cobalt Phthalocyanine Complexes. *J. Phys. Chem. C* **2013**, *117*, 23664–23675.

(30) Wang, Q.; Li, H.; Yang, J. H.; Sun, Q.; Li, Q.; Yang, J. Iron Phthalocyanine-Graphene Donor-Acceptor Hybrids for Visible-Light-Assisted Degradation of Phenol in the Presence of H₂O₂. *Appl. Catal., B* **2016**, *192*, 182–192.

(31) Beregovaya, I. V.; Shchegoleva, L. N. Pseudorotation As a Mechanism for Intramolecular Electron Density Transfer. Fragmentation of the Octafluoronaphthalene Radical Anion. *J. Fluorine Chem.* **2014**, *163*, 1–6.

(32) Guo, Z.; Nie, H.; Yang, Z.; Hua, W.; Ruan, C.; Chan, D.; Ge, M.; Chen, X.; Huang, S. 3D CNTs/Graphene-S-Al₃Ni₂ Cathodes for High-Sulfur-Loading and Long-Life Lithium-Sulfur Batteries. *Adv. Sci.* **2018**, *5*, 1800026.

(33) Zhou, T.; Lv, W.; Li, J.; Zhou, G.; Zhao, Y.; Fan, S.; Liu, B.; Li, B.; Kang, F.; Yang, Q. Twinborn TiO₂-TiN Heterostructures Enabling Smooth Trapping-Diffusion-Conversion of Polysulfides towards Ultralong Life Lithium-Sulfur Batteries. *Energy Environ. Sci.* **2017**, *10*, 1694–1703.

(34) Hua, W.; Yang, Z.; Nie, H.; Li, Z.; Yang, J.; Guo, Z.; Ruan, C.; Chen, X.; Huang, S. Polysulfide-Scission Reagents for the Suppression of the Shuttle Effect in Lithium-Sulfur Batteries. *ACS Nano* **2017**, *11*, 2209–2218.

(35) Xiao, Z.; Yang, Z.; Nie, H.; Lu, Y.; Yang, K.; Huang, S. Porous Carbon Nanotubes Etched by Water Steam for High-Rate Large-Capacity Lithium-Sulfur Batteries. *J. Mater. Chem. A* **2014**, *2*, 8683–8689.

(36) Xiao, Z.; Yang, Z.; Li, Z.; Li, P.; Wang, R. Synchronous Gains of Areal and Volumetric Capacities in Lithium-Sulfur Batteries Promised by Flower-Like Porous Ti₃C₂T_x Matrix. *ACS Nano* **2019**, *13*, 3404–3412.

(37) Wang, L.; Yang, Z.; Nie, H.; Gu, C.; Hua, W.; Xu, X.; Chen, X.; Chen, Y.; Huang, S. A Lightweight Multifunctional Interlayer of Sulfur-Nitrogen Dual-Doped Graphene for Ultrafast, Long-Life Lithium-Sulfur Batteries. *J. Mater. Chem. A* **2016**, *4*, 15343–15352.

(38) Pan, D.; Wang, S.; Zhao, B.; Wu, M.; Zhang, H.; Wang, Y.; Jiao, Z. Li Storage Properties of Disordered Graphene Nanosheets. *Chem. Mater.* **2009**, *21*, 3136–3142.

(39) Wu, J.; Rui, X.; Wang, C.; Pei, W. B.; Lau, R.; Yan, Q.; Zhang, Q. Nanostructured Conjugated Ladder Polymers for Stable and Fast Lithium Storage Anodes with High-Capacity. *Adv. Energy Mater.* **2015**, *5*, 1402189–1402193.

(40) Busche, M. R.; Drossel, T.; Leichtweiss, T.; Weber, D. A.; Falk, M.; Schneider, M.; Reich, M. L.; Sommer, H.; Adelhelm, P.; Janek, J. Dynamic Formation of a Solid-Liquid Electrolyte Interphase and Its Consequences for Hybrid-Battery Concepts. *Nat. Chem.* **2016**, *8*, 426–434.

(41) Lai, Y.; Nie, H.; Xu, X.; Fang, G.; Ding, X.; Chan, D.; Zhou, S.; Zhang, Y.; Chen, X.; Yang, Z. Interfacial Molecule Mediators in Cathodes for Advanced Li-S Batteries. *ACS Appl. Mater. Interfaces* **2019**, *11*, 29978–29984.

(42) Hou, T. Z.; Xu, W. T.; Chen, X.; Peng, H. J.; Huang, J. Q.; Zhang, Q. Lithium Bond Chemistry in Lithium-Sulfur Batteries. *Angew. Chem., Int. Ed.* **2017**, *56*, 8178–8182.

(43) Zeng, Y.; Li, X.; Zhang, X.; Zheng, S.; Meng, L. Insight Into the Nature of the Interactions of Furan and Thiophene with Hydrogen Halides and Lithium Halides: *Ab Initio* and QTAIM Studies. *J. Mol. Model.* **2011**, *17*, 2907–2918.

(44) Li, X.; Zeng, Y.; Zhang, X.; Zheng, S.; Meng, L. Insight Into the Lithium/Hydrogen Bonding in (CH₂)₂X··LiY/HY (X: C = CH₂, O, S; Y = F, Cl, Br) Complexes. *J. Mol. Model.* **2011**, *17*, 757–767.

(45) Hou, T. Z.; Chen, X.; Peng, H. J.; Huang, J. Q.; Li, B. Q.; Zhang, Q.; Li, B. Design Principles for Heteroatom-Doped Nanocarbon to Achieve Strong Anchoring of Polysulfides for Lithium-Sulfur Batteries. *Small* **2016**, *12*, 3283–3291.

(46) Demir-Cakan, R.; Morcrette, M.; Nouar, F.; Davoisne, C.; Devic, T.; Gonbeau, D.; Dominko, R.; Serre, C.; Ferey, G.; Tarascon, J. M. Cathode Composites for Li-S Batteries via the Use of Oxygenated Porous Architectures. *J. Am. Chem. Soc.* **2011**, *133*, 16154–16160.

(47) Zheng, J.; Tian, J.; Wu, D.; Gu, M.; Xu, W.; Wang, C.; Gao, F.; Engelhard, M. H.; Zhang, J. G.; Liu, J.; Xiao, J. Lewis Acid-Base Interactions Between Polysulfides and Metal Organic Framework in Lithium Sulfur Batteries. *Nano Lett.* **2014**, *14*, 2345–2352.

(48) Liu, F.; Wang, C.; Sui, X.; Riaz, M. A.; Xu, M.; Wei, L.; Chen, Y. Synthesis of Graphene Materials by Electrochemical Exfoliation: Recent Progress and Future Potential. *Carbon Energy* **2019**, *1*, 173–199.

(49) Fu, Y.; Wu, Z.; Yuan, Y.; Chen, P.; Yu, L.; Yuan, L.; Han, Q.; Lan, Y.; Bai, W.; Kan, E.; Huang, C.; Ouyang, X.; Wang, X.; Zhu, J.; Lu, J. Switchable Encapsulation of Polysulfides in the Transition between Sulfur and Lithium Sulfide. *Nat. Commun.* **2020**, *11*, 845.

(50) Huang, W.; Lin, Z.; Liu, H.; Na, R.; Tian, J.; Shan, Z. Enhanced Polysulfide Redox Kinetics Electro-Catalyzed by Cobalt Phthalocyanine for Advanced Lithium-Sulfur Batteries. *J. Mater. Chem. A* **2018**, *6*, 17132–17141.

(51) Dillard, C.; Singh, A.; Kalra, V. Polysulfide Speciation and Electrolyte Interactions in Lithium-Sulfur Batteries with *In Situ* Infrared Spectroelectrochemistry. *J. Phys. Chem. C* **2018**, *122*, 18195–18203.

(52) Yuan, G.; Zhang, G.; Zhou, Y.; Yang, F. Synergetic Adsorption and Catalytic Oxidation Performance Originating from Leafy Graphite Nanosheet Anchored Iron(ii) Phthalocyanine Nanorods for Efficient Organic Dye Degradation. *RSC Adv.* **2015**, *5*, 26132–26140.

(53) He, C.; Wu, Z.; Zhao, L.; Ming, M.; Zhang, Y.; Yi, Y.; Hu, J. Identification of FeN₄ As an Efficient Active Site for Electrochemical N₂ Reduction. *ACS Catal.* **2019**, *9*, 7311–7317.

(54) Fan, J.; Trenary, M. Symmetry and the Surface Infrared Selection Rule for the Determination of the Structure of Molecules on Metal Surfaces. *Langmuir* **1994**, *10*, 3649–3657.

(55) Chan, D.; Xiao, Z.; Guo, Z.; Lai, Y.; Zhang, Y.; Zhou, S.; Ding, X.; Nie, H.; Yang, Z. Titanium Silicalite As a Radical-Redox Mediator for High-Energy-Density Lithium-Sulfur Batteries. *Nanoscale* **2019**, *11*, 16968–16977.

(56) Xu, N.; Qian, T.; Liu, X.; Liu, J.; Chen, Y.; Yan, C. Greatly Suppressed Shuttle Effect for Improved Lithium Sulfur Battery Performance through Short Chain Intermediates. *Nano Lett.* **2017**, *17*, 538–543.

(57) Kim, B.; Park, S. *In Situ* Spectroelectrochemical Studies on the Reduction of Sulfur in Dimethyl Sulfoxide Solution. *J. Electrochem. Soc.* **1993**, *140*, 115–122.

(58) Deng, Z.; Zhang, Z.; Lai, Y.; Liu, J.; Li, J.; Liu, Y. Electrochemical Impedance Spectroscopy Study of a Lithium/Sulfur Battery: Modeling and Analysis of Capacity Fading. *J. Electrochem. Soc.* **2013**, *160*, A553–A558.

(59) Tan, G.; Xu, R.; Xing, Z.; Yuan, Y.; Lu, J.; Wen, J.; Liu, C.; Ma, L.; Zhan, C.; Liu, Q.; Wu, T.; Jian, Z.; Shahbazian-Yassar, R.; Ren, Y.; Miller, D. J.; Curtiss, L. A.; Ji, X.; Amine, K. Burning Lithium in CS₂

for High-Performing Compact Li_2S -Graphene Nanocapsules for Li-S Batteries. *Nat. Energy* **2017**, *2*, 17090.

(60) Iskandar, F.; Setiawan, B.; Mayangsari, T. R.; Maharsi, R.; Purwanto, A.; Aimon, A. H. Electrochemical Impedance Analysis of Polyvinylpyrrolidone-Coated Sulfur/Reduced Graphene Oxide (S/rGO) Electrode. *Mater. Res. Express* **2019**, *6*, 025514.

(61) Peng, H.; Hou, T.; Zhang, Q.; Huang, J.; Cheng, X.; Guo, M.; Yuan, Z.; He, L.; Wei, F. Strongly Coupled Interfaces between a Heterogeneous Carbon Host and a Sulfur-Containing Guest for Highly Stable Lithium-Sulfur Batteries: Mechanistic Insight into Capacity Degradation. *Adv. Mater. Interfaces* **2014**, *1*, 1400227.

(62) Blum, V.; Gehrke, R.; Hanke, F.; Havu, P.; Havu, V.; Ren, X.; Reuter, K.; Scheffler, M. *Ab Initio* Molecular Simulations with Numeric Atom-Centered Orbitals. *Comput. Phys. Commun.* **2009**, *180*, 2175–2196.

(63) Kresse, G.; Joubert, D. From Ultrasoft Pseudopotentials to the Projector Augmented-Wave Method. *Phys. Rev. B: Condens. Matter Mater. Phys.* **1999**, *59*, 1758–1775.

(64) Perdew, J. P.; Burke, K.; Ernzerhof, M. Generalized Gradient Approximation Made Simple. *Phys. Rev. Lett.* **1996**, *77*, 3865–3868.

(65) Tkatchenko, A.; Scheffler, M. Accurate Molecular Van der Waals Interactions from Ground-State Electron Density and Free-Atom Reference Data. *Phys. Rev. Lett.* **2009**, *102*, 073005.

(66) Mulliken, R. S. Electronic Population Analysis on LCAO-MO Molecular Wave Functions. II. Overlap Populations, Bond Orders, and Covalent Bond Energies. *J. Chem. Phys.* **1955**, *23*, 1841–1846.